

Interpretable Convolutional Neural Networks

Quanshi Zhang, Ying Nian Wu, and Song-Chun Zhu
University of California, Los Angeles

Abstract

This paper proposes a method to modify traditional convolutional neural networks (CNNs) into interpretable CNNs, in order to clarify knowledge representations in high conv-layers of CNNs. In an interpretable CNN, each filter in a high conv-layer represents a certain object part. Our interpretable CNNs use exactly the same training data as ordinary CNNs without a need for additional annotations of object parts or textures for supervision. The interpretable CNN automatically assigns each filter in a high conv-layer with an object part during the learning process. Our method can be applied to different types of CNNs with different structures. The clear knowledge representation in an interpretable CNN can help people understand logics inside a CNN, i.e. what patterns are memorized by the CNN for prediction. Experiments have showed that filters in an interpretable CNN are more semantically meaningful than those in traditional CNNs.

1. Introduction

Convolutional neural networks (CNNs) [12, 10, 7] have achieved superior performance in many visual tasks, such as object classification and detection. However, the interpretability of the model is always an Achilles' heel of neural networks, which has presented great challenges for neural networks for decades.

In this paper, we focus on a new problem, i.e. *can we learn a CNN whose knowledge representations in conv-layers are interpretable?* We expect the CNN itself has a certain introspection of its own knowledge representations, so that the CNN can regularize its representations to ensure high interpretability during the end-to-end learning process. This is different from conventional off-line visualization [25, 13, 19, 4, 5, 16] and diagnosis [2, 9, 11, 14] of representations in pre-trained CNNs.

Bau *et al.* [2] defined six kinds of semantics in CNNs, i.e. *objects, parts, scenes, textures, materials, and colors*. In fact, we can roughly summarize these semantics into two types. We can consider the first two semantics as patterns of object parts and regard the last four semantics as certain

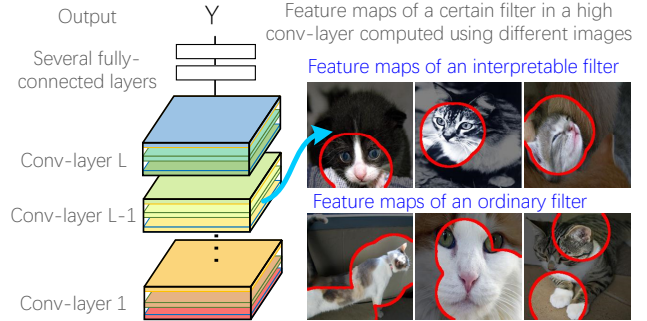


Figure 1. Comparison of a filter's feature maps in an interpretable CNN and those in a traditional CNN.

textures. Moreover, filter in low conv-layers usually represent simple textures, whereas filters in high conv-layers are more likely to represent object parts.

Therefore, in this study, we aim to train each filter in a high conv-layer to clearly represent an object part. Fig. 1 shows the key difference between traditional CNNs and our interpretable CNNs. In traditional CNNs, a high-layer filter may represent a mixture of patterns, i.e. the filter may be activated by both the head part and the leg part of a cat. Such complex knowledge representations in high conv-layers greatly decrease the interpretability of the network. In contrast, the filter in our interpretable CNN is activated by a certain part.

In this way, we can explicitly identify which object parts are memorized in the CNN for classification without ambiguity. The goal of this study can be summarized as follows.

- 1 We propose to slightly revise CNNs to improve their interpretability, which can be broadly applied to CNNs with different network structures.
- 2 We do **not** need annotations of object parts and/or textures to ensure each high-layer filter to have a certain semantic meaning. We hope that each filter automatically learns a meaningful object-part representation without any additional human supervision.
- 3 When we modify a traditional CNN to an interpretable CNN, we do not change experimental settings for learning. i.e. the interpretable CNN does not change

the previous loss function on the top layer and uses exactly the same training samples.

- 4 The design for interpretability may decrease the discriminative power of the network a bit, but we hope to limit such a decrease within a small range.

Methods: Given a high conv-layer in a CNN, we propose a simple yet effective loss for each filter in the conv-layer to push the filter towards the representation of an object part. As shown in Fig. 2, we add a local loss for the output feature map of each filter. The loss encourages a low entropy of inter-category activations and a low entropy of spatial distributions of neural activations. *I.e.* each filter must encode a distinguishable object part that is exclusively contained by a single object category, and the filter’s activations must be well localized at a single object part, rather than repetitively appear on different regions of the same object. For example, the left eye and the right eye may be represented using two different part filters, because contexts of the two eyes are symmetric, but not the same. Here, we assume that repetitive shapes on different regions are more prone to describe low-level textures (*e.g.* local colors and/or edges), instead of high-level parts.

The value of network interpretability: The clear semantics in high conv-layers is of great value when we need human beings to trust a computer’s prediction. Although the CNN can achieve high accuracy on different tasks, human beings usually cannot fully trust a computer, unless it can clearly explain its logics for decisions, *i.e.* what patterns are contained in CNNs for prediction. Given an image, current studies for network diagnosis [5, 16, 14] localize image regions that contribute most to network predictions at the pixel level. In this study, we expect the CNN to explain its logics at the object-part level. Given a well trained interpretable CNN, we can explicitly show the part semantics of each filter, as well as the distribution of object parts in each category that are memorized by the CNN for object classification.

Contributions: In this paper, we focus on a new task, *i.e.* end-to-end learning a CNN whose knowledge representations in high conv-layers are interpretable. We propose a simple yet effective method that is able to modify different types of CNNs into interpretable CNNs without any additional annotations of object parts or textures for supervision. Experiments showed that our method significantly improved the object-part interpretability of CNNs.

2. Related work

Interpretability and discriminability are two important aspects of a model [2]. In recent years, different methods are developed to explore the semantics hidden inside a CNN. Many statistical methods [22, 24, 1] have been proposed to analyze the characteristics of CNN features.

Network visualization: Visualization of filters in a CNN is the most direct way of exploring the pattern hidden inside a neural unit. [25, 13, 19] showed the appearance that maximized the score of a given unit. up-convolutional nets [4] were used to invert CNN feature maps to images.

Pattern retrieval: Going beyond passive visualization, some studies actively retrieve certain units from CNNs for different applications. Like middle-level feature extraction [21] in images, pattern retrieval mainly learns mid-level representations of CNN knowledge. Zhou *et al.* [29, 30] selected units from feature maps to describe “scenes”. Simon *et al.* discovered objects from feature maps of unlabeled images [17], and selected a certain filter to describe each semantic part in a supervised fashion [18]. However, most methods either ignored the case that a filter of high conv-layers encoded a mixture of patterns or did not disentangle the mixture of patterns in a single filter. [27] extracted certain neural units from a filter’s feature map to describe an object part in an weakly-supervised manner. [6] used a gradient-based method to interpret visual question-answering models.

Model diagnosis: Many methods have been developed to diagnose representations of a black-box model. The LIME method proposed by Ribeiro *et al.* [14], influence functions [9] and gradient-based visualization methods [5, 16] extracted key image regions that were responsible for each network output, in order to interpret network representations.

These methods require people to manually check key regions for the prediction on each testing image. In contrast, the interpretable CNN itself can automatically describe parts that are used for decisions during the CNN inference procedure. Similarly, some approaches aim to evaluate all potential representations of all images in a category. Lakkaraju *et al.* [11] and Zhang *et al.* [28] explored unknown knowledge hidden in CNNs via active annotations and active question-answering.

Learning a better representation: Unlike above methods diagnosing and/or visualizing a pre-trained CNN, we more focus on the problem of how to make a CNN learn a more meaningful representation. [15] required people to label dimensions of input features that were related to each output according to common sense, in order to learn a better model. Hu *et al.* [8] designed a number of logic rules for network outputs, and used these rules to regularize the learning of neural networks. In this study, we invent a generic method to regularize knowledge representation of a filter towards representations of object parts.

3. Algorithm

Given a target conv-layer of a CNN, each filter in the conv-layer should only be activated by a certain object part of a certain category, and keep inactivated on images of

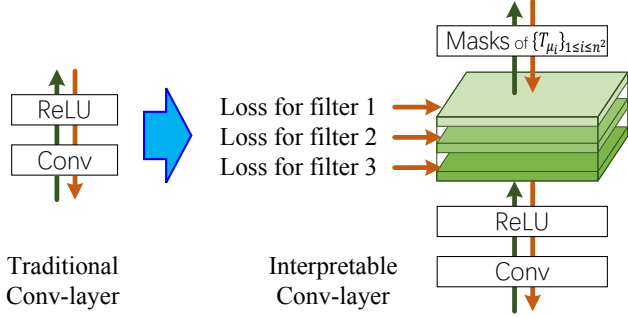


Figure 2. Structures of an ordinary conv-layer and an interpretable conv-layer. Green and red lines indicate the forward and backward propagations, respectively.

other categories. Let \mathbf{I} denote a set of training images, where $\mathbf{I}_c \subset \mathbf{I}$ represents the subset of training images that belongs to category c , ($c = 1, 2, \dots, C$). We can use different types of losses to learn CNNs for multi-class classification, single-class classification (*i.e.* $c = 1$ for images of a category and $c = 2$ for random images), and other tasks.

As shown in Fig. 2, we add a loss to each filter f . $\mathbf{X} = \{x | x = f(I), I \in \mathbf{I}\}$ denotes feature maps of the filter f after an ReLU operation that are computed on different training images, $x_{ij} \geq 0$. The feature map $x \in \mathbf{X}$ of each image $I \in \mathbf{I}$ is an $n \times n$ matrix.

Let us assume a filter f describe an object part of category c . We expect the feature map x to be strongly activated in images of category c and keep silent on other images. Therefore, as shown in Fig. 3, we use a number of templates $\mathbf{T} = \{T^-, T_{\mu_1}, T_{\mu_2}, \dots, T_{\mu_{n^2}}\}$ to evaluate the fitness between the current feature map x and the ideal distribution of activations *w.r.t.* its semantics. Each template is an $n \times n$ matrix. If the image I belongs to \mathbf{I}_c , the feature map x is expected to fit a positive template T^+ ; otherwise, we hope that the feature map x well matches a negative template T^- . More specifically, given an input image $I \in \mathbf{I}_c$, the corresponding positive template $T^+ = T_\mu$ for the category c is determined by its part location $\mu \in (i, j)$, $1 \leq i, j \leq n$, *i.e.* the neural unit x_{ij} in x that potentially corresponds to the part. Because each feature map is supposed to be highly related to a certain template, we formulate the loss as the mutual information between \mathbf{X} and \mathbf{T} .

$$\begin{aligned} \text{Loss}_f &= -MI(\mathbf{X}; \mathbf{T}) \quad \text{for filter } f \\ &= -\sum_T p(T) \sum_x p(x|T) \log \frac{p(x|T)}{p(x)} \end{aligned} \quad (1)$$

We expect the feature map to have a high mutual information with its corresponding template, *i.e.* we hope the actual feature map x well fit the corresponding template T . As shown in Fig. 3, the template is a matrix with the same size of the feature map x . We consider the part template T_μ as the filter's ideal neural activations when the corresponding

part is localized at μ .

The prior probability of a template is given as

$$p(T_\mu) = \frac{\alpha}{n^2}, \quad p(T^-) = 1 - \alpha \quad (2)$$

where α is a constant that denotes the prior likelihood of positive templates. We define the conditional likelihood $p(x|T)$ given a template T as

$$\forall T \in \mathbf{T}, \quad p(x|T) = \frac{1}{Z_T} \exp [tr(x \cdot T)] \quad (3)$$

where $Z_T = \sum_{x \in \mathbf{X}} \exp(tr(x \cdot T))$. $x \cdot T$ indicates the multiplication between x and T ; $tr(\cdot)$ indicates the trace of a matrix. $p(x) = \sum_T p(T)p(x|T)$.

In addition, during the forward propagation, we also use the best part template T_μ as a mask to filter out signals in the feature map x , *i.e.* we compute $\hat{\mu} = \arg\max_{[i,j]} x_{ij}$ and $x^{\text{new}} = \max\{x^{\text{old}} \circ T_{\hat{\mu}}, 0\}$, where \circ denotes the element-wise multiplication. The filter is physically encoded in the CNN, *i.e.* we uniformly apply signal masks to all feature maps, no matter whether the input image belongs to the target category c or not. The design of masks also supports the gradient back-propagation for end-to-end learning.

Determining the target category for each filter: It is very important to determine a target category for each filter to select a mask during the forward propagation process and to compute gradients in Eqn. (5) during the back-propagation process. In this paper, we simply assign the filter with the category \hat{c} whose images activate the filter most, *i.e.* $\hat{c} = \arg\max_c \text{mean}_{x: I \in \mathbf{I}_c} \sum_{ij} x_{ij}$.

Part templates: As shown in Fig. 3, a negative template is given as $T^- = (t_{ij}^-)$, $t_{ij}^- = -\tau < 0$, where τ is a positive constant. The positive template corresponding to μ is formulated as $T_\mu = (t_{ij}^+)$, $t_{ij}^+ = \tau \cdot \max(1 - \beta \frac{\|[i,j] - \mu\|_1}{n}, -1)$, where $\|\cdot\|_1$ denotes the L-1 norm distance; n is the size of the feature map; β is a constant parameter.

3.1. Learning

We train the interpretable CNN via an end-to-end manner. During the forward-propagation process, each filter in the CNN passes its information in a bottom-up manner, just like traditional CNNs. During the back-propagation process, each filter in an interpretable conv-layer receives gradients *w.r.t.* its feature map x from both the upper layer and the local loss Loss_f .

$$\left(\frac{\partial \text{Loss}}{\partial x_{ij}}\right)^{\text{new}} = \lambda \frac{\partial \text{Loss}_f}{\partial x_{ij}} + \frac{1}{N} \sum_{i=1}^N \frac{\partial \mathbf{L}(\hat{y}_i, y_i^*)}{\partial x_{ij}} \quad (4)$$

where λ is a weight. We use the new loss in the back-propagation process to update CNN parameters.

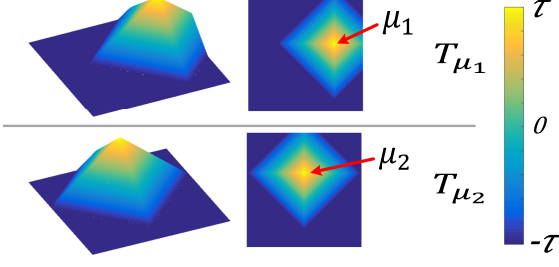


Figure 3. Templates of T_{μ_i} . In fact, the algorithm also supports us to define a round template T_{μ_i} by using the L-2 norm distance. Here, we use the L-1 norm distance instead to speed up the computation.

We compute gradients of Loss_f w.r.t. each element x_{ij} of feature map x as follows¹.

$$\begin{aligned} \frac{\partial \text{Loss}_f}{\partial x_{ij}} &= \frac{1}{Z_T} \sum_T p(T) t_{ij} e^{tr(x \cdot T)} \left\{ tr(x \cdot T) - \log [Z_T p(x)] \right\} \\ &\approx \frac{p(\hat{T}) t_{ij}}{Z_{\hat{T}}} e^{tr(x \cdot \hat{T})} \left\{ tr(x \cdot \hat{T}) - \log Z_{\hat{T}} - \log p(x) \right\} \end{aligned} \quad (5)$$

where \hat{T} is the target template for feature map x . If the given image I belongs to the target category of filter f , $\hat{T} = T_{\hat{\mu}}$. $\hat{\mu}$ denotes the part location estimated as the neural unit with the strongest activation, $\hat{\mu} = \text{argmax}_{[i,j]} x_{ij}$. If image I belongs to other categories, $\hat{T} = T^-$. Considering that $e^{tr(x \cdot \hat{T})} \gg e^{tr(x \cdot T)}$, $\forall T \in \mathbf{T} \setminus \{\hat{T}\}$ after initial learning episodes, we make the above approximation to simplify the computation. Because Z_T is computed using numerous feature maps, we can roughly treat Z_T as a constant to compute gradients computation in the above equation. We gradually update the value of Z_T during the training process². Similarly, we can also approximate $p(x)$ without huge computation².

4. Understanding of the loss

In fact, the loss in Eqn. (1) can be re-written as¹

$$\begin{aligned} \text{Loss}_f &= -H(\mathbf{T}) + H(\mathbf{T}' = \{T^-, \mathbf{T}^+\} | \mathbf{X}) \\ &\quad + \sum_x p(\mathbf{T}^+, x) H(\mathbf{T}^+ | X = x) \end{aligned} \quad (6)$$

In the above equation, the first term $H(\mathbf{T}^+) = -\sum_{T \in \mathbf{T}^+} p(T | \mathbf{T}^+) \log p(T | \mathbf{T}^+)$ is a constant, where $\mathbf{T}^+ = \{T_{\mu_1}, T_{\mu_2}, \dots, T_{\mu_{n_2}}\} \subset \mathbf{T}$. This term denotes the prior entropy of \mathbf{T}^+ .

¹Please see the proof in the appendix.

²We can use a subset of feature maps to approximate the value of Z_T , and continue to update Z_T when we receive more feature maps during the training process. Similarly, we can approximate $p(x)$ using a subset of feature maps. We compute $p(x) = \sum_T p(T) p(x | T) = \sum_T p(T) \frac{\exp[tr(x \cdot T)]}{Z_T} \approx \sum_T p(T) \text{mean}_x \frac{\exp[tr(x \cdot T)]}{Z_T}$.

Low inter-category entropy: The second term $H(\mathbf{T}' = \{T^-, \mathbf{T}^+\} | \mathbf{X})$ is computed as

$$H(\mathbf{T}' = \{T^-, \mathbf{T}^+\} | \mathbf{X}) = - \sum_x p(x) \sum_{T \in \{T^-, \mathbf{T}^+\}} p(T | x) \log p(T | x) \quad (7)$$

which encourages a low conditional entropy of inter-category activations, *i.e.* a well-learned filter f needs to be exclusively activated by a certain category c and keep silent on other categories. In other words, we can use a feature map x of f to identify whether the input image belongs to category c or not. Here, we define the set of all positive templates \mathbf{T}^+ as a single label, which represents category c . We use the negative template T^- to denote other categories. We set $p(\mathbf{T}^+) = \sum_{\mu} p(T_{\mu})$ to compute $H(\mathbf{T}' = \{T^-, \mathbf{T}^+\} | \mathbf{X})$. **Low spatial entropy:** The third term in Eqn. (6) is given as

$$H(\mathbf{T}^+ | X = x) = \sum_{\mu} \tilde{p}(T_{\mu} | x) \log \tilde{p}(T_{\mu} | x) \quad (8)$$

where $\tilde{p}(T_{\mu} | x) = \frac{p(T_{\mu} | x)}{p(\mathbf{T}^+ | x)}$. This term encourages a low conditional entropy of spatial distribution of x 's activations. Given an image $I \in \mathbf{I}_c$, a well-learned filter should only be activated by a single region $\hat{\mu}$ of the feature map x , instead of repetitively appearing at different locations.

5. Experiments

In experiments, we used object images in three different benchmark datasets to learn four types of interpretable CNNs for single-category classification and multi-category classification. We visualized feature maps of filters in interpretable conv-layers to demonstrate semantic meanings of these filters. We used two types of metrics to evaluate the clarity of the part semantics of a convolutional filter, and we compared the interpretability between filters in ordinary CNNs and those in interpretable CNNs. Experiments showed that filters in our interpretable CNNs were much more semantically meaningful than those in ordinary CNNs.

Three benchmark datasets: Because we needed ground-truth annotations of landmark object parts to evaluate the semantic clarity of the learned convolutional filters, we chose three benchmark datasets with part annotations for training and testing, which included the ILSVRC 2013 DET Animal-Part dataset [27], the CUB200-2011 dataset [23], and the Pascal VOC Part dataset [3]. As discussed in [3, 27], animals usually contain non-rigid parts, which presents a key challenge for part localization. Thus, we followed [3, 27] to select the 37 animal categories in the three datasets for evaluation.

All the three datasets provide ground-truth bounding boxes of entire objects. For part annotations, the ILSVRC 2013 DET Animal-Part dataset [27] contains ground-truth bounding boxes of the head and the leg parts of 30 animal

categories. The CUB200-2011 dataset [23] contains a total of 11.8K bird images of 200 species, and the dataset provides center positions of 15 bird parts. The six animal categories in the Pascal VOC Part dataset [3] contains ground-truth segmentations of 107 types of object parts.

Four types of CNNs: In order to demonstrate the broad applicability of our interpretable CNN, we modified four typical CNNs, *i.e.* the AlexNet [10], the VGG-M [20], the VGG-S [20], the VGG-16 [20], into interpretable CNNs. Considering that skip connections in residual networks [7] usually make a single feature map encode patterns of different filters, in this study, we did not test the performance on residual networks to simplify the story. Given a certain CNN structure, we modified all filters in the top conv-layer of the ordinary network into interpretable ones. Then, we inserted a new conv-layer with M filters above the original top conv-layer, where M is the channel number of the input of the new conv-layer. We also set filters in the new conv-layer as interpretable ones. Each filter was a $3 \times 3 \times M$ tensor with a bias term. We added zero padding to input feature maps, so that output feature maps were of the same size as input feature maps.

Implementation details: We set parameters as $\tau = \frac{0.5}{n^2}$, $\alpha = \frac{n^2}{1+n^2}$, and $\beta = 4$. We updated weights of filter losses *w.r.t.* magnitudes of neural activations in an online manner, $\lambda = 5 \times 10^{-6} \text{mean}_{x \in \mathbf{X}} \max_{i,j} x_{ij}$. When we learned an interpretable CNN for animals in datasets of [27, 23, 3], we initialized parameters for fully-connected layers and the new conv-layer, and loaded conv-layer parameters from a non-interpretable CNN that was pre-trained using 1.2M ImageNet images in [10, 20]. We then fine-tuned the interpretable CNN using training images in the dataset.

5.1. Experiments

Single-category classification: We learned the four types of interpretable CNNs based on the AlexNet, VGG-M, VGG-S, and VGG-16 structures for each category in the ILSVRC 2013 DET Animal-Part dataset [27], the CUB200-2011 dataset [23], and the Pascal VOC Part dataset [3]. Besides, we also learned ordinary AlexNet, VGG-M, VGG-S, and VGG-16 networks using the same training data of each category for comparison. We used the logistic loss for single-category classification. Just like the learning of CNNs in [27, 28, 26], we cropped image regions inside object bounding boxes of the target category as positive samples, and the ground-truth label of a positive sample is defined as $y^* = +1$. We regarded images of other categories as negative samples with ground-truth labels $y^* = -1$.

Multi-category classification: We used the six animal categories in the Pascal VOC Part dataset [3] to learn CNNs for multi-category classification. We learned four interpretable CNNs based on the AlexNet, VGG-M, VGG-S, and VGG-16 structures. Ordinary AlexNet, VGG-M,

VGG-S, and VGG-16 networks were also learned for multi-category classification as baselines. To simplify the implementation, we also used the logistic loss for multi-category classification. We trained each category output of the CNN using an independent logistic loss. We followed the same method in the above paragraph to prepare positive object samples for each category.

5.2. Evaluation metric

As discussed in [2], filters in low conv-layers usually represent simple patterns or object details (*e.g.* edges, simple textures, and colors), whereas filters in high conv-layers are more likely to represent complex large-scale object parts. Thus, it is more meaningful and challenging to ensure clear semantics in high conv-layers than in low conv-layers.

In experiments, we evaluated the clarity of part semantics for filters in the top conv-layer of each CNN. We used the following two metrics for evaluation.

5.2.1 Part interpretability

We followed the metric proposed by Bau *et al.* [2] to measure the object-part interpretability of filters. We briefly introduce this evaluation metric as follows. For each filter f , we computed its final output feature maps \mathbf{X} after ReLU/mask operations on different input images. Then, the distribution of neural activation scores in all positions of all feature maps $\{x_{ij}\}$ was computed. Only neural activations with top scores were considered as valid representations of the filter’s semantics. *I.e.* [2] set an activation threshold T_f such that $p(x_{ij} > T_f) = 0.005$ for all spatial locations $[i, j]$ of all feature maps $x \in \mathbf{X}$. All feature map regions, whose activation scores exceeded the threshold T_f , were selected as valid feature map regions for evaluation.

In order to associate low-resolution feature map regions with image-resolution ground-truth part segmentations, feature maps were scaled up to the image resolution using bilinear interpolation by backward propagating x_{ij} ’s receptive fields to the image plane. We used S_f^I to denote the scaled-up valid map regions of filter f on image I .

The compatibility between each filter f and the k -th part on image I was reported as an intersection-over-union score.

$$IoU_{f,k}^I = \frac{S_f^I \cap S_k^I}{S_f^I \cup S_k^I} \quad (9)$$

where S_k^I denotes the ground-truth mask of the k -th part on image I . Just like in [2], the $IoU_{f,k}^I$ score was only computed for images containing ground-truth masks of the k -th part.

Given an image I , we associated filter f with the k -th part if $IoU_{f,k}^I > 0.2$. Note that the criterion of $IoU_{f,k}^I > 0.2$ for part association is much stricter than $IoU_{f,k}^I > 0.04$

	bird	cat	cow	dog	horse	sheep	Avg.
AlexNet	0.319	0.354	0.331	0.368	0.301	0.359	0.339
AlexNet, interpretable	0.749	0.603	0.602	0.603	0.716	0.637	0.652
VGG-16	0.524	0.479	0.492	0.538	0.434	0.559	0.504
VGG-16, interpretable	0.824	0.646	0.674	0.851	0.780	0.799	0.762
VGG-M	0.349	0.357	0.347	0.361	0.327	0.360	0.350
VGG-M, interpretable	0.812	0.595	0.604	0.599	0.715	0.703	0.671
VGG-S	0.252	0.263	0.236	0.269	0.229	0.289	0.256
VGG-S, interpretable	0.510	0.375	0.275	0.448	0.459	0.239	0.384

Table 1. Average part interpretability of filters in CNNs that are trained for single-category classification using the Pascal VOC Part dataset [3].

that was used in [2]. It is because compared to other CNN semantics discussed in [2] (such as colors and textures), the object-part semantics usually requires a stricter criterion.

We computed the probability of the k -th part being associating with the filter f as $P_{f,k} = \text{mean}_{I:\text{with } k\text{-th part}} \mathbf{1}(IoU_{f,k}^I > 0.2)$. Note that one filter might be associated with multiple object parts in an image. Among all parts, we reported the highest probability of part association as the object part of filter f , i.e. $P_f = \max_k P_{f,k}$.

For single-category classification, we used testing images of the target category for evaluation. In the Pascal VOC Part dataset [3], we used four parts for the *bird* category. We merged ground-truth regions of the head, beak, and l/r-eyes as the head part, merged regions of the torso, neck, and l/r-wings as the torso part, merged regions of l/r-legs/feet as the leg part, and used tail regions as the fourth part. We used five parts for the *cat* category. We merged regions of the head, l/r-eyes, l/r-ears, and nose as the head part, merged regions of the torso and neck as the torso part, merged regions of frontal l/r-legs/paws as the frontal legs, merged regions of back l/r-legs/paws as the back legs, and used the tail as the fifth part. We used four parts for the *cow* category, which were defined in a similar way to the cat category. We added l/r-horns to the head part and omitted the tail part. We defined five parts for the *dog* category in the same way as the cat category. We defined four parts for both the *horse* and *sheep* categories in the same way as the cow category. We computed the average part interpretability P_f over all filters for evaluation.

For multi-category classification, we first identified a target category \hat{c} for each filter f as the category that activated the filter most, i.e. $\hat{c} = \text{argmax}_c \text{mean}_{x:I \in \mathcal{I}_c} \sum_{i,j} x_{ij}$. Then, we computed the object-part interpretability using images of category \hat{c} based on object parts, as introduced above.

5.2.2 Location stability

The second metric measures the stability of part locations. Given a feature map x of filter f , we regarded the unit $\hat{\mu}$ with the highest activation as the location inference of the

Network	Avg. location deviation
VGG-16	0.738
VGG-16, interpretable	0.929
VGG-M	0.489
VGG-M, interpretable	0.765
VGG-S	0.507
VGG-S, interpretable	0.575

Table 2. Average part interpretability of filters in CNNs that are trained for multi-category classification. Filters in our interpretable CNNs exhibited significantly better part interpretability than other CNNs in all comparisons.

filter, i.e. $\hat{\mu} = \text{argmax}_{[i,j]} x_{ij}$. We assumed that if the filter f consistently represented the same object part through different objects, then distances between the inferred part location $\hat{\mu}$ and some landmark object parts should not change a lot among different objects. For example, if a filter represented the shoulder part, then the distance between the shoulder and the head should keep stable through different objects. Let $d_I(p_k, \hat{\mu}) = \frac{\|\mathbf{p}_k - \mathbf{p}(\hat{\mu})\|}{\sqrt{w^2 + h^2}}$ denote the distance between the inferred part and the k -th landmark part \mathbf{p}_k on image I , where $\mathbf{p}(\hat{\mu})$ denotes the inferred position on the image plane when we backward propagate the receptive field of neural unit $\hat{\mu}$ to the image plane. As in [27, 18], the distance was normalized using the diagonal length of the input image $\sqrt{w^2 + h^2}$.

For single-category classification, we evaluated the location stability of each filter f as follows. We used $D_{f,k} = \sqrt{\text{var}_I[d_I(p_k, \hat{\mu})]}$ to evaluate the *location deviation level* of filter f w.r.t. the k -th landmark part, where $\text{var}_I[d_I(p_k, \hat{\mu})]$ is referred to as the variation of the distance $d_I(p_k, \hat{\mu})$. Note that each landmark part could not appear in all testing images. Therefore, for each filter f , we only used its top-100 inference results with the highest activation scores of $x_{\hat{\mu}}$ on images containing the k -th landmark part to compute $D_{f,k}$. Thus, we used the average location deviation of all the filters in a conv-layer w.r.t. all landmark parts, i.e. $\text{mean}_f \text{mean}_{k=1}^K D_{f,k}$, to measure the location instability of the filter, where K denotes the number of landmark parts.

More specifically, landmark object parts for each category were selected as follows. For each testing image in the ILSVRC 2013 DET Animal-Part dataset [27], we used the *head* and *frontal legs* of each category as landmark parts for evaluation. For the Pascal VOC Part dataset [3], we computed the distances between the inferred position $\hat{\mu}$ and positions of the *head*, *neck*, and *torso* parts. For the CUB200-2011 dataset [23], we used ground-truth positions of the *head*, *back*, *tail* of birds as landmarks for computation. We selected these object parts as landmarks, because these parts appeared on testing samples most frequently.

For multi-category classification, we needed to determine two terms for each filter f , i.e. 1) which category filter f mainly represented and 2) the location devi-

AlexNet	gold.	bird	frog	turt.	liza.	koala	lobs.	dog	fox	cat	lion	tiger	bear	rabb.	hams.	squi.
AlexNet, interpretable	0.227	0.235	0.215	0.216	0.247	0.180	0.173	0.204	0.202	0.209	0.193	0.200	0.203	0.209	0.181	0.211
VGG-16	0.118	0.134	0.127	0.151	0.137	0.111	0.109	0.131	0.123	0.134	0.118	0.126	0.134	0.134	0.109	0.134
VGG-16, interpretable	0.216	0.219	0.203	0.212	0.240	0.179	0.178	0.202	0.194	0.208	0.196	0.203	0.201	0.206	0.176	0.212
VGG-M	0.107	0.140	0.121	0.162	0.159	0.099	0.119	0.108	0.097	0.121	0.094	0.136	0.114	0.111	0.092	0.091
VGG-M, interpretable	0.227	0.234	0.213	0.216	0.248	0.180	0.176	0.205	0.205	0.212	0.197	0.204	0.203	0.211	0.180	0.211
VGG-S	0.124	0.124	0.126	0.152	0.140	0.112	0.104	0.127	0.115	0.146	0.111	0.126	0.143	0.136	0.116	0.134
VGG-S, interpretable	0.223	0.234	0.210	0.214	0.244	0.179	0.175	0.202	0.201	0.208	0.195	0.201	0.201	0.209	0.180	0.207
AlexNet	horse	zebra	swine	hippo	catt.	sheep	ante.	camel	otter	arma.	monk.	elep.	red pa.	gia.pa.		Avg.
AlexNet, interpretable	0.214	0.218	0.199	0.199	0.203	0.218	0.208	0.215	0.224	0.226	0.196	0.177	0.198	0.177		0.206
VGG-16	0.139	0.118	0.128	0.125	0.137	0.142	0.119	0.144	0.147	0.134	0.126	0.120	0.119	0.103		0.128
VGG-16, interpretable	0.212	0.216	0.199	0.197	0.198	0.211	0.203	0.210	0.217	0.229	0.192	0.182	0.201	0.177		0.203
VGG-M	0.149	0.109	0.132	0.117	0.143	0.137	0.128	0.148	0.131	0.140	0.104	0.118	0.095	0.089		0.120
VGG-M, interpretable	0.213	0.223	0.198	0.198	0.201	0.219	0.206	0.218	0.226	0.228	0.198	0.177	0.201	0.179		0.207
VGG-S	0.133	0.112	0.134	0.119	0.130	0.132	0.108	0.147	0.144	0.131	0.121	0.122	0.125	0.096		0.126
VGG-S, interpretable	0.210	0.219	0.196	0.197	0.199	0.219	0.201	0.217	0.223	0.222	0.198	0.176	0.196	0.177		0.204
	0.135	0.112	0.129	0.124	0.133	0.142	0.109	0.144	0.148	0.132	0.127	0.121	0.110	0.101		0.127

Table 3. Average location deviation of filters in CNNs that are trained for single-category classification using the ILSVRC 2013 DET Animal-Part dataset [27]. Filters in our interpretable CNNs exhibited significantly better localization stability than ordinary CNNs in all comparisons.

	bird	cat	cow	dog	horse	sheep	Avg.
AlexNet	0.216	0.185	0.199	0.180	0.204	0.197	0.197
AlexNet, interpretable	0.127	0.125	0.127	0.124	0.122	0.124	0.125
VGG-16	0.204	0.188	0.205	0.179	0.202	0.202	0.197
VGG-16, interpretable	0.143	0.138	0.149	0.104	0.137	0.141	0.135
VGG-M	0.214	0.186	0.202	0.183	0.205	0.200	0.198
VGG-M, interpretable	0.121	0.133	0.127	0.123	0.118	0.118	0.123
VGG-S	0.214	0.184	0.199	0.181	0.203	0.199	0.197
VGG-S, interpretable	0.125	0.129	0.130	0.122	0.121	0.124	0.125

Table 4. Average location deviation of filters in CNNs that are trained for single-category classification using the Pascal VOC Part dataset [3]. Filters in our interpretable CNNs exhibited significantly better localization stability than other CNNs in all comparisons.

Network	Avg. location deviation
AlexNet	0.212
AlexNet, interpretable	0.099
VGG-16	0.194
VGG-16, interpretable	0.107
VGG-M	0.208
VGG-M, interpretable	0.091
VGG-S	0.209
VGG-S, interpretable	0.103

Table 5. Average location deviation of filters in CNNs that are trained for single-category classification using the CUB200-2011 [23].

ation level $D_{f,k}$ w.r.t. each landmark part of f 's target category. Because filters in ordinary CNNs were usually not exclusively represent a single category, we simply assigned filter f with the category whose landmark parts can achieve the lowest location deviation to simplify the com-

Network	Avg. location deviation
VGG-16	0.181
VGG-16, interpretable	0.103
VGG-M	0.190
VGG-M, interpretable	0.116
VGG-S	0.195
VGG-S, interpretable	0.109

Table 6. Average location deviation of filters in CNNs that are trained for multi-category classification. Filters in our interpretable CNNs exhibited significantly better localization stability than other CNNs in all comparisons.

	multi-category	single-category		
		ILSVRC Part [27]	Pascal VOC Part [3]	CUB200-2011 [23]
AlexNet	–	96.28%	95.40%	95.59%
AlexNet, interpretable	–	95.38%	93.93%	95.35%
VGG-M	93.88%	97.34%	96.82%	97.34%
VGG-M, interpretable	96.19%	95.77%	94.17%	96.03%
VGG-S	94.05%	97.62%	97.74%	97.24%
VGG-S, interpretable	96.78%	95.64%	95.47%	95.82%
VGG-16	97.97%	98.58%	98.66%	98.91%
VGG-16, interpretable	98.50%	96.67%	95.39%	96.51%

Table 7. Classification accuracy on different datasets. In single-category classification, ordinary CNNs performed better, while in multi-category classification, interpretable CNNs exhibited superior performance.

putation. Thus, we computed the average location deviation as $\text{mean}_f \min_c \text{mean}_{k \in \text{Part}_c} D_{f,k}$, where Part_c denotes the set of part indexes belonging to category c .

5.3. Experimental results and analysis

Fig. 4 visualizes filters in top conv-layers of CNNs, which were trained for single-category classification. We showed the feature map S_f^I of a filter for visualization,

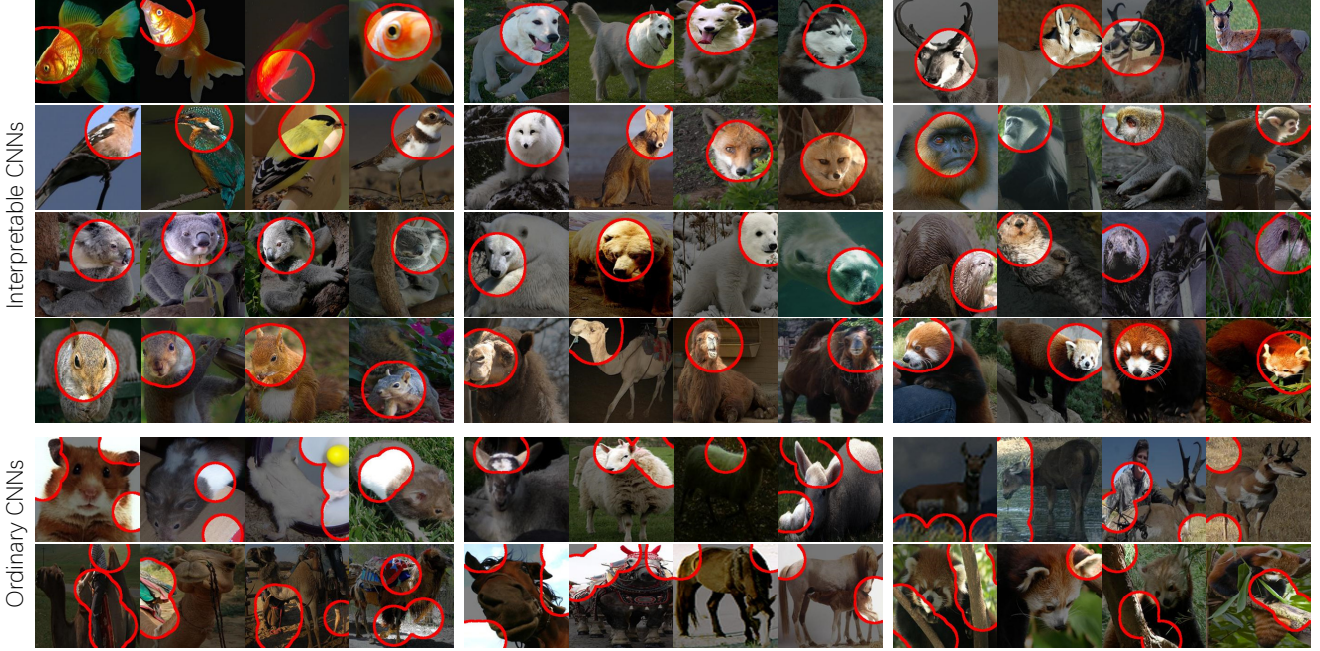


Figure 4. Visualization of filters in top conv-layers. We used the scaled up feature maps S_f^I of a filter for visualization. The top four rows visualize filters in interpretable CNNs, and the bottom two rows correspond to filters in ordinary CNNs. We found that interpretable CNNs usually encoded head patterns of animals in its top conv-layer for classification.

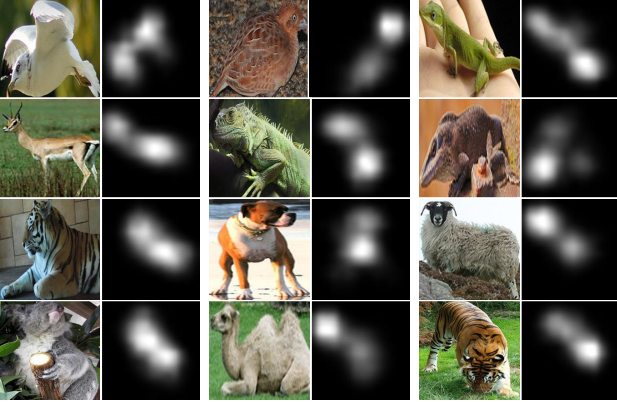


Figure 5. Heat maps for distributions of object parts that are encoded in interpretable filters. We use all filters in the top conv-layer to compute the heat map.

which was scaled up to the image resolution. Filters in interpretable CNNs were mainly activated by a certain object part, whereas filters in ordinary CNNs did not have clear semantic meanings. Fig. 5 shows heat maps for distributions of object parts detected by interpretable filters. Interpretable CNNs usually selectively modeled most discriminative object parts and ignored other parts.

Tables 1 and 2 compare part interpretability of CNNs learned for single-category classification and that of CNNs learned for multi-category classification, respectively. Tables 3, 4, and 5 list average location deviations of CNNs

for single-category classification. Table 6 compares average location deviations of CNNs for multi-category classification. Our interpretable CNNs exhibited much higher interpretability and much better location stability than ordinary CNNs in all comparisons. Table 7 compares classification accuracy of different CNNs. Ordinary CNNs performed better in single-category classification. Whereas, for multi-category classification, interpretable CNNs exhibited superior performance to ordinary CNNs. The good performance in multi-category classification is because that our interpretable filters are suitable to encode object parts of a category, rather than noises in random images.

6. Conclusion and discussions

In this paper, we have proposed a general method to modify traditional CNNs to enhance the interpretability of CNNs. As discussed in [2], besides the discriminative power, the interpretability is another important property of a network. We design certain losses to regularize filters in high conv-layers without additional annotations for supervision. These losses push each target filter towards the representation of an object part of a category. Experiments have showed that our interpretable CNNs encoded more semantically meaningful knowledge in high conv-layers than traditional CNNs.

When we use an interpretable CNN to simultaneously classify a large number of categories, filters in a conv-layer are separated for different categories. Without sufficient fil-

ters for each category, the CNN’s classification accuracy may decrease a bit. Moreover, in this study, we require a filter to strictly represent a single object part. In future work, we will design new filters to describe discriminative textures of a category and new filters for object parts that are shared by multiple categories, in order to achieve a higher model flexibility.

References

- [1] M. Aubry and B. C. Russell. Understanding deep features with computer-generated imagery. *In ICCV*, 2015. 2
- [2] D. Bau, B. Zhou, A. Khosla, A. Oliva, and A. Torralba. Network dissection: Quantifying interpretability of deep visual representations. *In CVPR*, 2017. 1, 2, 5, 6, 8
- [3] X. Chen, R. Mottaghi, X. Liu, S. Fidler, R. Urtasun, and A. Yuille. Detect what you can: Detecting and representing objects using holistic models and body parts. *In CVPR*, 2014. 4, 5, 6, 7
- [4] A. Dosovitskiy and T. Brox. Inverting visual representations with convolutional networks. *In CVPR*, 2016. 1, 2
- [5] R. C. Fong and A. Vedaldi. Interpretable explanations of black boxes by meaningful perturbation. *In arXiv:1704.03296v1*, 2017. 1, 2
- [6] Y. Goyal, A. Mohapatra, D. Parikh, and D. Batra. Towards transparent ai systems: Interpreting visual question answering models. *In arXiv:1608.08974v2*, 2016. 2
- [7] K. He, X. Zhang, S. Ren, and J. Sun. Deep residual learning for image recognition. *In CVPR*, 2016. 1, 5
- [8] Z. Hu, X. Ma, Z. Liu, E. Hovy, and E. P. Xing. Harnessing deep neural networks with logic rules. *In arXiv:1603.06318v2*, 2016. 2
- [9] P. Koh and P. Liang. Understanding black-box predictions via influence functions. *In ICML*, 2017. 1, 2
- [10] A. Krizhevsky, I. Sutskever, and G. Hinton. Imagenet classification with deep convolutional neural networks. *In NIPS*, 2012. 1, 5
- [11] H. Lakkaraju, E. Kamar, R. Caruana, and E. Horvitz. Identifying unknown unknowns in the open world: Representations and policies for guided exploration. *In AAAI*, 2017. 1, 2
- [12] Y. LeCun, L. Bottou, Y. Bengio, and P. Haffner. Gradient-based learning applied to document recognition. *In Proceedings of the IEEE*, 1998. 1
- [13] A. Mahendran and A. Vedaldi. Understanding deep image representations by inverting them. *In CVPR*, 2015. 1, 2
- [14] M. T. Ribeiro, S. Singh, and C. Guestrin. “why should i trust you?” explaining the predictions of any classifier. *In KDD*, 2016. 1, 2
- [15] A. S. Ross, M. C. Hughes, and F. Doshi-Velez. Right for the right reasons: Training differentiable models by constraining their explanations. *In arXiv:1703.03717v1*, 2017. 2
- [16] R. R. Selvaraju, M. Cogswell, A. Das, R. Vedantam, D. Parikh, and D. Batra. Grad-cam: Visual explanations from deep networks via gradient-based localization. *In arXiv:1610.02391v3*, 2017. 1, 2
- [17] M. Simon and E. Rodner. Neural activation constellations: Unsupervised part model discovery with convolutional networks. *In ICCV*, 2015. 2
- [18] M. Simon, E. Rodner, and J. Denzler. Part detector discovery in deep convolutional neural networks. *In ACCV*, 2014. 2, 6
- [19] K. Simonyan, A. Vedaldi, and A. Zisserman. Deep inside convolutional networks: visualising image classification models and saliency maps. *In arXiv:1312.6034*, 2013. 1, 2
- [20] K. Simonyan and A. Zisserman. Very deep convolutional networks for large-scale image recognition. *In ICLR*, 2015. 5
- [21] S. Singh, A. Gupta, and A. A. Efros. Unsupervised discovery of mid-level discriminative patches. *In ECCV*, 2012. 2
- [22] C. Szegedy, W. Zaremba, I. Sutskever, J. Bruna, D. Erhan, I. Goodfellow, and R. Fergus. Intriguing properties of neural networks. *In arXiv:1312.6199v4*, 2014. 2
- [23] C. Wah, S. Branson, P. Welinder, P. Perona, and S. Belongie. The caltech-ucsd birds-200-2011 dataset. Technical report, In California Institute of Technology, 2011. 4, 5, 6, 7
- [24] J. Yosinski, J. Clune, Y. Bengio, and H. Lipson. How transferable are features in deep neural networks? *In NIPS*, 2014. 2
- [25] M. D. Zeiler and R. Fergus. Visualizing and understanding convolutional networks. *In ECCV*, 2014. 1, 2
- [26] Q. Zhang, R. Cao, F. Shi, Y. Wu, and S.-C. Zhu. Interpreting cnn knowledge using an explanatory graph. *In arXiv 1708.01785*, 2017. 5
- [27] Q. Zhang, R. Cao, Y. N. Wu, and S.-C. Zhu. Growing interpretable graphs on convnets via multi-shot learning. *In AAAI*, 2016. 2, 4, 5, 6, 7
- [28] Q. Zhang, R. Cao, Y. N. Wu, and S.-C. Zhu. Mining part concepts from cnns via active question-answering. *In CVPR*, 2017. 2, 5
- [29] B. Zhou, A. Khosla, A. Lapedriza, A. Oliva, and A. Torralba. Object detectors emerge in deep scene cnns. *In ICRL*, 2015. 2
- [30] B. Zhou, A. Khosla, A. Lapedriza, A. Oliva, and A. Torralba. Learning deep features for discriminative localization. *In CVPR*, 2016. 2

Appendix

Proof of equations

$$\begin{aligned}
\frac{\partial \text{Loss}}{\partial x_{ij}} &= - \sum_{T \in \mathbf{T}} p(T) \left\{ \frac{\partial p(x|T)}{\partial x_{ij}} [\log p(x|T) - \log p(x) + 1] - p(x|T) \frac{\partial \log p(x)}{\partial x_{ij}} \right\} \\
&= - \sum_{T \in \mathbf{T}} p(T) \left\{ \frac{\partial p(x|T)}{\partial x_{ij}} [\log p(x|T) - \log p(x) + 1] - p(x|T) \frac{1}{p(x)} \frac{\partial p(x)}{\partial x_{ij}} \right\} \\
&= - \sum_{T \in \mathbf{T}} p(T) \left\{ \frac{\partial p(x|T)}{\partial x_{ij}} [\log p(x|T) - \log p(x) + 1] - p(x|T) \frac{1}{p(x)} \sum_{T'} \left[p(T') \frac{\partial p(x|T')}{\partial x_{ij}} \right] \right\} \\
&= - \sum_{T \in \mathbf{T}} p(T) \left\{ \frac{\partial p(x|T)}{\partial x_{ij}} [\log p(x|T) - \log p(x) + 1] \right\} \\
&\quad + \sum_{T \in \mathbf{T}} p(T) \frac{\partial p(x|T)}{\partial x_{ij}} \frac{\sum_{T'} p(T') p(x|T')}{p(x)} \quad // \text{ swap roles of } T \text{ and } T' \\
&= - \sum_{T \in \mathbf{T}} p(T) \left\{ \frac{\partial p(x|T)}{\partial x_{ij}} [\log p(x|T) - \log p(x) + 1] \right\} + \sum_{T \in \mathbf{T}} p(T) \frac{\partial p(x|T)}{\partial x_{ij}} \\
&= - \sum_{T \in \mathbf{T}} \frac{\partial p(x|T)}{\partial x_{ij}} p(T) [\log p(x|T) - \log p(x)] \\
&= - \sum_{T \in \mathbf{T}} \frac{t_{ij} p(T) e^{tr(x \cdot T)}}{Z_T} \left\{ tr(x \cdot T) - \log [Z_T p(x)] \right\}
\end{aligned}$$

$$\begin{aligned}
\text{Loss} &= - MI(\mathbf{X}; \mathbf{T}) \quad // \mathbf{T} = \{T^-, T_{\mu_1}, T_{\mu_2}, \dots, T_{\mu_{n_2}}\} \\
&= - H(\mathbf{T}) + H(\mathbf{T}|\mathbf{X}) \\
&= - H(\mathbf{T}) - \sum_x p(x) \sum_{T \in \mathbf{T}} p(T|x) \log p(T|x) \\
&= - H(\mathbf{T}) - \sum_x p(x) \left\{ p(T^-|x) \log p(T^-|x) + \sum_{\mu} p(T_{\mu}|x) \log p(T_{\mu}|x) \right\} \\
&= - H(\mathbf{T}) - \sum_x p(x) \left\{ p(T^-|x) \log p(T^-|x) + \sum_{\mu} p(T_{\mu}|x) \log \left[\frac{p(T_{\mu}|x)}{p(\mathbf{T}^+|x)} p(\mathbf{T}^+|x) \right] \right\} \quad // p(\mathbf{T}^+|x) = \sum_{\mu} p(T_{\mu}|x) \\
&= - H(\mathbf{T}) - \sum_x p(x) \left\{ p(T^-|x) \log p(T^-|x) + p(\mathbf{T}^+|x) \log p(\mathbf{T}^+|x) + \sum_{\mu} p(T_{\mu}|x) \log \frac{p(T_{\mu}|x)}{p(\mathbf{T}^+|x)} \right\} \\
&= - H(\mathbf{T}) + H(\mathbf{T}' = \{T^-, \mathbf{T}^+\}|\mathbf{X}) + \sum_x p(\mathbf{T}^+, x) H(\mathbf{T}^+ = \{T_{\mu}\}|X = x)
\end{aligned}$$

where

$$H(\mathbf{T}'' = \{T_{\mu}\}|X = x) = \sum_{\mu} \tilde{p}(T_{\mu}|X = x) \log \tilde{p}(T_{\mu}|X = x), \quad \tilde{p}(T_{\mu}|X = x) = \frac{p(T_{\mu}|x)}{p(\mathbf{T}^+|x)}$$

Visualization of CNN filters



Figure 6. Visualization of filters in the top interpretable conv-layer. Each row corresponds to feature maps of a filter in a CNN that is learned to classify a certain category.



Figure 7. Visualization of filters in the top interpretable conv-layer. Each row corresponds to feature maps of a filter in a CNN that is learned to classify a certain category.



Figure 8. Visualization of filters in the top conv-layer of an ordinary CNN. Each row corresponds to feature maps of a filter in a CNN that is learned to classify a certain category.